Versatile Three-Dimensional Virus-Based Template for Dye-Sensitized Solar Cells with Improved Electron Transport and Light Harvesting

Po-Yen Chen,[†,‡,▽] Xiangnan Dang,[‡,§,▽] Matthew T. Klug,[‡,⊥] Jifa Qi,[‡,§] Noémie-Manuelle Dorval Courchesne,[†,‡] Fred J. Burpo,[∥] Nicholas Fang,[⊥] Paula T. Hammond,[†,‡,*] and Angela M. Belcher[‡,§,∥,*]

[†]Department of Chemical Engineering, Massachusetts Institute of Technology, Cambridge, Massachusetts 02139, United States, [‡]The David H. Koch Institute for Integrative Cancer Research, Massachusetts Institute of Technology, Cambridge, Massachusetts 02139, United States, [§]Department of Materials Science and Engineering, Massachusetts Institute of Technology, Cambridge, Massachusetts 02139, United States, [⊥]Department of Mechanical Engineering, Massachusetts Institute of Technology, Cambridge, Massachusetts 02139, United States, and [∥]Department of Biological Engineering, Massachusetts Institute of Technology, Cambridge, Massachusetts 02139, United States [▽]These authors contributed equally.

ABSTRACT By genetically encoding affinity for inorganic materials into the capsid proteins of the M13 bacteriophage, the virus can act as a template for the synthesis of nanomaterial composites for use in various device applications. Herein, the M13 bacteriophage is employed to build a multifunctional and three-dimensional scaffold capable of improving both electron collection and light harvesting in dye-sensitized solar cells (DSSCs). This has been accomplished by binding gold nanoparticles (AuNPs) to the virus proteins and encapsulating the AuNP–virus complexes in TiO_2 to produce a plasmon-enhanced and nanowire (NW)-based photoanode. The NW morphology exhibits an improved electron diffusion length compared to traditional nanoparticle-based DSSCs, and the AuNPs increase the light absorption of the dye-molecules through the phenomenon of localized surface plasmon resonance. Consequently, we report a virus-templated and plasmon-enhanced DSSC with an efficiency of 8.46%, which is achieved through optimizing both the NW morphology and the concentration of AuNPs loaded into the solar cells. In addition, we propose a theoretical model that predicts the experimentally observed trends of plasmon enhancement.

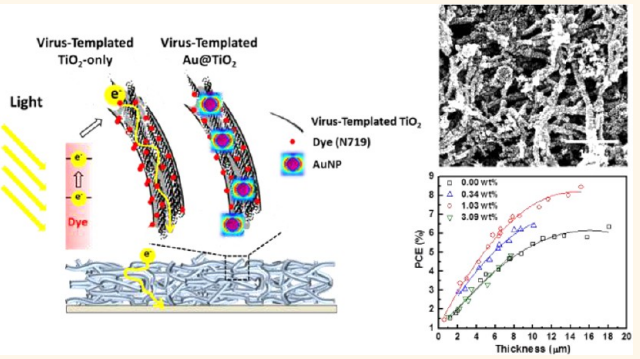

KEYWORDS: M13 bacteriophage · biotemplate · three-dimensional network · dye-sensitized solar cells · electron transport · light harvesting · localized surface plasmon resonance

Meeting the ever-growing need of affordable clean energy requires the development of inexpensive and environmentally friendly synthesis routes that are capable of producing efficient energy conversion devices. Using biological or polymeric materials as templates enables the assembly of hybrid materials at the nanoscale using aqueous-based and low-temperature synthesis. One particularly versatile biotemplate is the M13 bacteriophage, a filamentous virus that is 880 nm in length and 6.5 nm in diameter. It has demonstrated the ability to assemble or nucleate a broad range of materials, including metals,[1] semiconductors,[2] polymers,[3] carbon nanotubes,[4] and metal oxides.[4] Through genetic engineering of the surface coat proteins, the targeted materials can be assembled along the virus surface to produce functional materials with two-[5] or three-dimensional (3D) morphologies for various device applications, including fuel cells,[6] lithium ion batteries,[7,8] photocatalysts,[9] and photovoltaics.[4,10,11]

The dye-sensitized solar cell (DSSC) is a promising solution-processed photovoltaic technology.[12] The key components of a DSSC include dye-molecules converting photons into electron–hole pairs and nanoporous titanium dioxide (TiO_2) thin films

* Address correspondence to hammond@mit.edu, belcher@mit.edu.

Received for review November 20, 2012 and accepted June 29, 2013.

Published online June 29, 2013
10.1021/nn4014164

(photoanodes) transporting the photogenerated electrons. The power conversion efficiency (PCE) of DSSCs is mainly determined by the ability of photoanodes to harvest light and to collect electrons.[13] Generally, efficient light harvesting and electron collection require the consideration of many design criteria, including morphologies and materials. Nanostructures of TiO_2 with a high aspect ratio, such as nanorods,[14] nanotubes,[15] and nanofibers,[16] have been proven to be more efficient electron collectors than the randomly packed nanoparticle (NP) architecture commonly used in DSSC photoanodes. However, one-dimensional (1D) structures provide less surface area for the adsorption of dye, reducing light harvesting. To achieve efficient light harvesting, the development of highly absorbing dye-molecules or other mechanisms to increase optical absorption are required, such as light concentration with the localized surface plasmon resonance (LSPR) of noble metal NPs.[17−20] Therefore, different functional materials are required for separately improving electron collection and light harvesting.

Here, we report a novel 3D viral network as a versatile platform for DSSCs that can template TiO_2 nanowires (NWs) for efficient electron transport and can also bind AuNPs to incorporate them uniformly into the photoanodes for improved light harvesting of dye-molecules *via* LSPR. Templated by a cross-linked virus hydrogel scaffold, the TiO_2 NWs provide a direct pathway for electron transport from the photoexcited dyes to the current collector (Scheme 1) in the photoanode. The linear morphology yields an increased electron diffusion length (L_n) compared to conventional NP-based photoanodes. In addition, the M13 virus can bind AuNPs prior to the templated synthesis of TiO_2; the resulting TiO_2-coated AuNPs generate plasmons that improves the photoabsorption of dye-molecules adsorbed on the Au@TiO_2 nanocomposites (Scheme 1). As a result, the 3D plasmon-enhanced virus-templated photoanodes exhibit efficient electron collection and improved light absorption simultaneously. An optimized amount (1.03 wt %) of AuNPs homogeneously distributed throughout the virus-templated photoanode enhances the short-circuit current density (J_{SC}) from 10.97 to 13.72 mA cm^{-2} and improves the PCE from 6.03% to 8.46%. This is further investigated theoretically by developing a numerical model that calculates the electric field enhancement in the system. The proposed numerical model accurately captures the trend of variation of the PCE with the concentration of AuNPs.

RESULTS AND DISCUSSION

3D M13 Virus-Templated Photoanodes for Improved Electron Collection. To generate a 3D scaffold, a virus hydrogel network is first formed on a fluorine-doped tin oxide (FTO) using an aqueous glutaraldehyde solution as the cross-linking agent (Figure 1). Glutaraldehyde has a high reactivity with amine groups at a near-neutral pH and is able to cross-link amine groups together

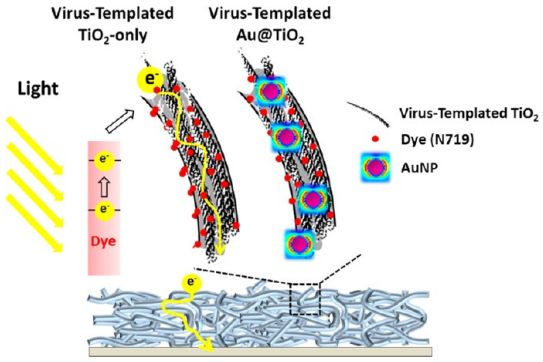

Scheme 1. Structures and mechanisms of DSSCs with the virus-templated TiO_2 and Au@TiO_2 photoanodes.

with thermally and chemically stable covalent bonds.[21] The virus solution (specific gravity, SG ≈ 1, pH = 7.4) is dropped onto the FTO substrate in a 1 cm^2 area defined by a 25-μm-thick Surlyn film spacer; the substrate is then placed upside-down on the surface of the glutaraldehyde solution (SG ≈ 1.1). As the glutaraldehyde diffuses across the fluid interface and upward into the virus solution, the amine groups on the virus coat proteins react with glutaraldehyde and stable covalent bonds between viruses are formed. After two hours of cross-linking, a virus hydrogel is spontaneously formed on the substrate.

After the virus hydrogel is achieved, the virus-templated TiO_2 NWs are formed directly on the substrate by a two-step aqueous phase nucleation method using solutions of TiO_2 precursors (*e.g.*, $TiCl_4$, $(NH_4)_2TiF_6$), which sequentially deposit a conformal thin TiO_2 layer on the virus template. The mechanism of the crystal growth of TiO_2 crystallites by hydrolysis of $TiCl_4$ is already well-understood.[22] During the hydrolysis of $TiCl_4$ at 50 °C (described in eq 1), the amorphous and anatase TiO_2 nanocrystallites, observed in X-ray diffraction (XRD) pattern (Figure S1), nucleate preferentially on the surface of the virus template due to the lower interfacial energy needed for the heterogeneous nucleation.

$$TiCl_4 + 2H_2O \rightarrow TiO_2 + 4HCl \quad (1)$$

A subsequent TiO_2 nucleation is introduced using $(NH_4)_2TiF_6$ and H_3BO_3 solution to reduce film cracking (imaged by scanning electron microscopy (SEM) in Figure S2); this reaction proceeds by the following mechanism described in eqs 2 and 3:

$$TiF_6^{2-} + 2H_2O \leftrightarrows TiO_2 + 4H^+ + 6F^- \quad (2)$$

$$BO_3^{3-} + 4F^- + 6H^+ \leftrightarrows BF_4^- + 3H_2O \quad (3)$$

Then, the resulting virus-templated TiO_2 structure is annealed at 500 °C for at least an hour, which provides enough heat and time to (1) remove the sacrificial virus scaffolds, (2) transform the amorphous/anatase nanocrystallites into anatase NPs (XRD analysis is shown in Figure 3(A)), and (3) sinter the NPs together into a percolative network.

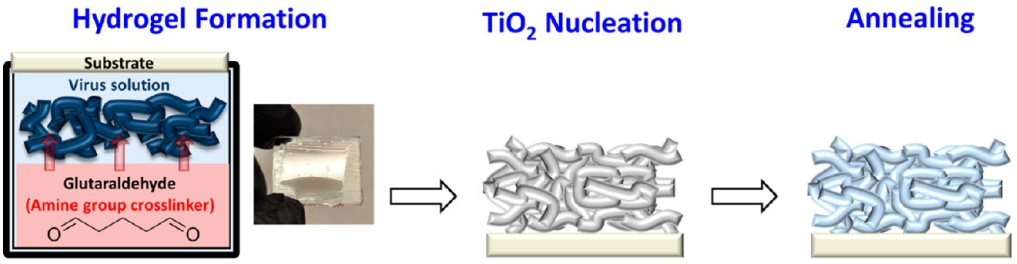

Figure 1. Schematic illustration of 3D porous TiO_2 photoanode fabrication process, including (1) hydrogel formation, (2) TiO_2 nucleation, and (3) annealing.

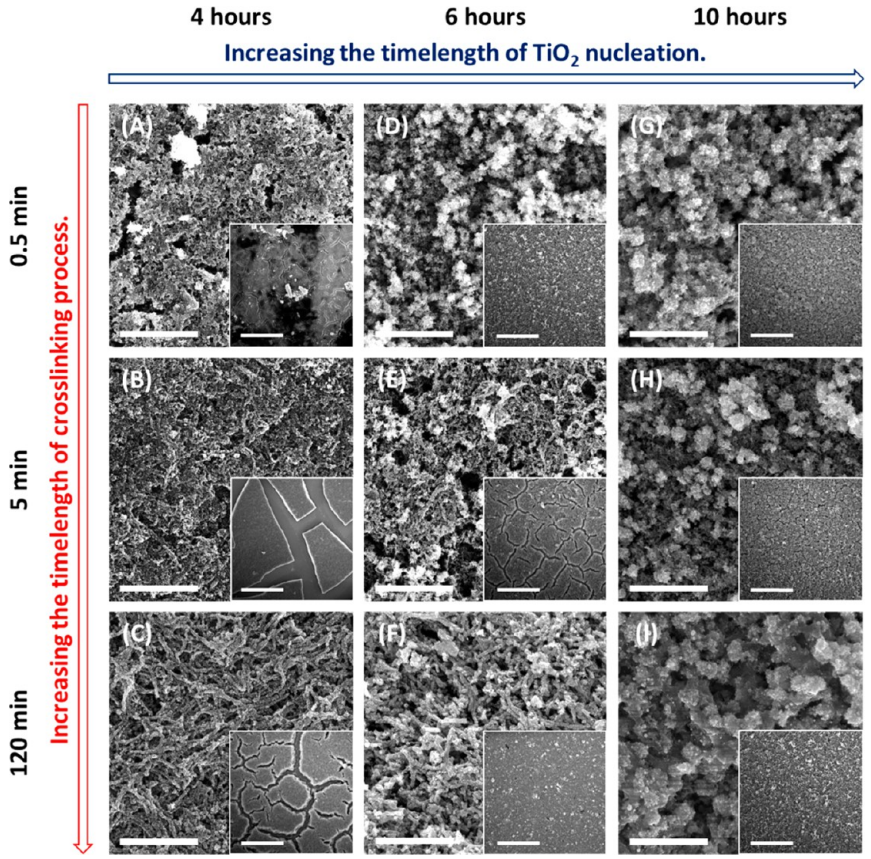

Figure 2. SEM images of the annealed TiO_2 photoanodes templated by virus hydrogels in different time lengths of cross-linking process and fabricated in different time lengths of TiO_2 nucleation. The scale bar is 2 μm, and the one in the inset is 30 μm. All of the films are sequentially nucleated with $(NH_4)_2TiF_6/H_3BO_3$ solution.

The aspect ratio of the NWs and the film quality mainly depend on the shape of the cross-linked viral hydrogel and the TiO_2 nucleation on the template. Therefore, three related parameters are tuned: (1) time length of the cross-linking process, (2) time length of the nucleation in the $TiCl_4$ solution, and (3) concentration of the $TiCl_4$ solution. First, the cross-linking process time affects the aspect ratio of the virus-templated NW. Longer cross-linking process times result in the formation of longer and denser viral bundles, leading to the formation of higher aspect ratio NWs in the photoanodes (SEM images are shown in Figure 2(C,F)). Also, longer nucleation times in the $TiCl_4$ solution result in the formation of more TiO_2 crystallites on the viral template. The thicker TiO_2 formation on the template can sustain the thermal tension experienced during the postanneal cooling process and thus reduce film cracking. However, when the nucleation period exceeds 10 hours, excessive particle nucleation leads to pore filling and random particle aggregation on the viral template (SEM images are shown in Figure 2(G–I)). In addition, the concentration of the $TiCl_4$ solution affects the TiO_2 nucleation and thus the film quality. As shown in Figure S3(A,B), a lower concentration of the $TiCl_4$ solution (0.04 and 0.1 M) gives rise to more crack-prone NW-based films. An optimal concentration (0.2 M) of the $TiCl_4$ solution produced a crack-free, yet interconnected

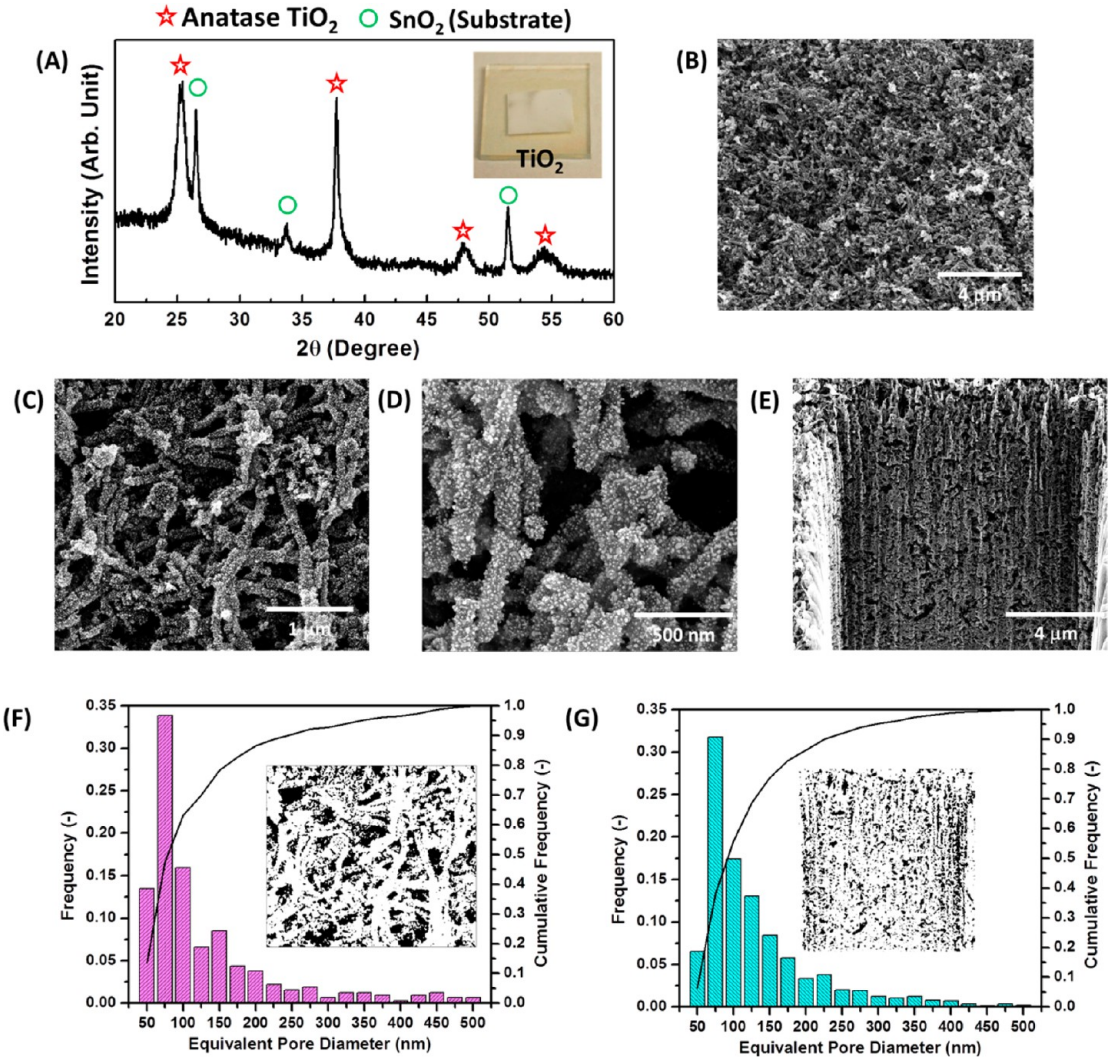

Figure 3. (A) XRD analysis of the annealed virus-templated anatase TiO_2 photoanodes. SEM images of the virus-templated TiO_2 photoanodes in (B−D) top-down view and (E) cross-section view. The pore size distributions calculated by the SEM images in (F) top-down view and (G) cross-section view, respectively.

virus-templated network, as shown in Figure S3(C). However, when the concentration of the $TiCl_4$ solution is increased to 0.4 M, larger particles are nucleated on the viral template, leading to lower aspect ratio wires and a reduced surface-to-volume ratio structure (Figure S3(D)).

After the virus-templated thin films are fabricated at the optimized condition (two-hour cross-linking, six-hour nucleation, and 0.2 M $TiCl_4$ solution), the as-obtained nanostructures are composed of tightly packed TiO_2 crystallites (~10 nm in diameter), forming interconnected porous NWs, which have been imaged by SEM in Figure 3(B,C) and transmission electron microscopy (TEM) in Figure 5**(F)**. Compared to the size of individual viral particles, the virus-templated TiO_2 NWs are approximately 150 nm in diameter and 2−3 μm in length (Figure 3(C,D)), which suggests that each NW in the photoanode is templated by a bundle of viruses. In addition, the mesoporous structure of the interconnected NW network persists throughout the 13-μm-thick film, providing directional pathways for improved electron transport (Figure 3(E)). Such a permeable matrix with interconnected pores maximizes interfacial contact with the electrolyte, thereby increasing the mobility of redox couples and minimizing back-recombination. In addition, the film porosity and the pore size distribution are investigated by analyzing the SEM images with an image analysis program (ImageJ). The porosities calculated from the top-down view (Figure 3(C)) and cross-section view (Figure 3(E)) SEM images are 51.4% and 48.0%, respectively. The porosity, which influences the overall performance by affecting the light absorption and electron diffusion, agrees well with the optimal porosity reported in the literature.[23] The pore size distributions (Figure 3(F,G)) are calculated from the top-down view and cross-section view SEM images as well. The equivalent pore diameter ranges from 50 to 500 nm, and the average pore diameter is 129.2 and 131.0 nm in both top-down view and cross-section view SEM images, respectively. It is noteworthy that both image

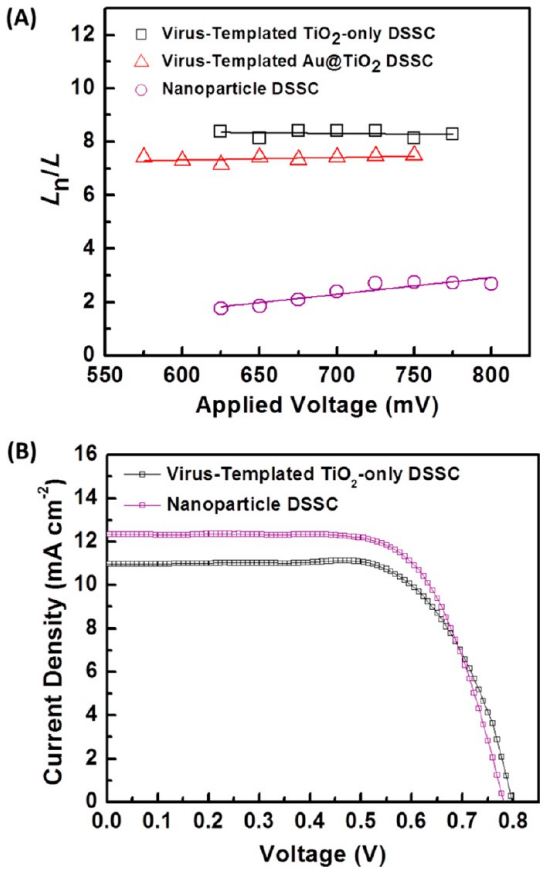

Figure 4. (A) Electron diffusion length analysis. L_n is the electron diffusion length, and L is the photoanode thickness. (B) Device performances for DSSCs employing the virus-templated TiO_2-only photoanodes. The performance of the NP-based DSSC is shown as a reference.

views give similar results for porosity, pore size distribution, and average pore diameter, which indicates that the porous structure is spatially uniform.

To demonstrate L_n and carrier collection of the 3D virus-templated TiO_2 photoanode, the electrochemical impedance spectra (EIS) are measured after the photoanodes are assembled with the electrolyte and counter electrodes. The L_n of different DSSC photoanodes calculated from EIS are shown in Figure 4(A), and the EIS diagrams and fitting results at 625 mV are also shown in Figure S4. These results along with the corresponding efficiency of electron collection (η_{COL}) are summarized in Table 1. The details of the calculation of L_n and η_{COL} are provided in the Supporting Information. As shown in Table 1, the device with the virus-templated photoanode exhibits a longer L_n (~8.4 times the film thickness) and higher η_{COL} (99.6%) than the commonly used TiO_2 NP-based DSSC (~1.8 times, 92.0%). These results indicate that the 3D TiO_2 network composed of interconnected NWs improves electron transport by lengthening electron lifetimes and reducing opportunities for interfacial recombination.

Furthermore, the device performance of the DSSC with a virus-templated TiO_2 photoanode is compared to that with a NP-based TiO_2 photoanode (Figure 4(B)), and the related photovoltaic parameters—open circuit voltage (V_{OC}), fill factor (FF), J_{SC}, PCE, and dye loading—are summarized in Table 1. The virus-templated DSSC demonstrates a PCE of 6.03% and a J_{SC} of 10.97 mA cm^{-2}, which are both lower than those of the TiO_2 NP-based DSSC (6.63% and 12.31 mA cm^{-2}), despite having a higher electron collection efficiency. Since the charge separation efficiency approaches unity when the N719 dye and TiO_2 are used, the decreased overall performance results from the reduced surface area, dye adsorption, and thus light harvesting ability of the 1D structure of the virus-templated TiO_2 NWs. In fact, the virus-templated device shows ~89.1% of J_{SC} with only ~73.5% of the dye loading (70.9 mmol cm^{-3}) compared to the NP-based solar cell (96.9 mmol cm^{-3}). Therefore, the virus-templated photoanodes composed of interconnected NWs exhibit efficient electron collection, while the randomly packed NP-based photoanode is advantageous for light harvesting. In order to compensate for the reduced dye adsorption in the virus-templated TiO_2 NW structure, strategies for improving the light-harvesting characteristics are designed.

M13 Virus as a Versatile Tool for Improved Light Harvesting. Localized surface plasmons (LSPs) are the elementary excited states of free electrons in metal NPs.[24] Physically, these are the collective oscillations of free electrons that arise at a metal−dielectric interface when excited by light near the resonance frequency. At resonance, the electrons generate a localized near-field, which effectively concentrates light into a thin region directly around the NP. Gold and silver NPs have resonances that occur in the visible range, making them particularly useful in enhancing light harvesting in various photovoltaic technologies.[25−27] The ability of M13 viruses to be programmed to bind with these noble metal NPs can thus be utilized to improve the optical absorption of the photoanodes in DSSCs. Once the viruses (TEM image in Figure 5(A)) and AuNPs (20 nm in diameter, TEM images in Figure 5(B)) are bound together through complexation in a colloidal suspension (TEM image in Figure 5(C)), the same photoanode fabrication process previously described can be performed with the AuNP−virus complexes. The morphology of the resulting virus-templated Au@TiO_2 structures is similar to that of the virus-templated TiO_2 films (SEM image in Figure S6). After the calcination of the virus-templated Au@TiO_2 photoanode, both Au and anatase TiO_2 peaks can be observed in the XRD pattern (Figure 5(D)). In addition, it is observed in the TEM images (Figure 5(E,F)) that ~10 nm TiO_2 crystallites are densely packed around the ~20 nm AuNPs, forming a protective shell, which prevents the AuNPs from promoting electron recombination and from being etched by the electrolyte.[20]

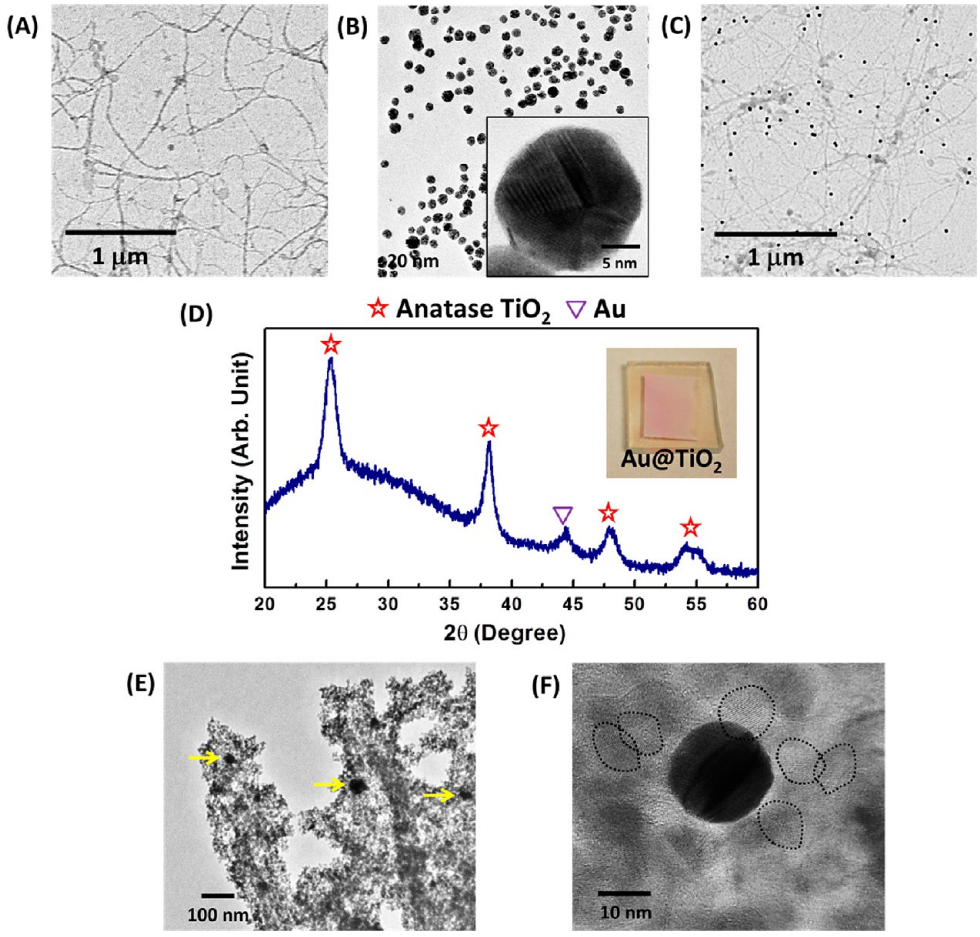

Figure 5. TEM images of (A) M13 virus, (B) as-synthesized 20 nm AuNPs, and (C) the AuNP−virus complex. (D) XRD analysis of the virus-templated anatase Au@TiO_2 photoanode. (E) TEM image of the annealed virus-templated Au@TiO_2 photoanode. The yellow arrows point out the 20 nm AuNPs embedded in TiO_2 crystallites. (F) High-resolution TEM image of 20 nm AuNP and 10 nm TiO_2 crystallites in the virus-templated Au@TiO_2 photoanodes. The black dashed circles show the crystallized TiO_2 particles in the photoanodes.

TABLE 1. Relevant Solar Cell Parameters Obtained from the Devices in Figure 4(A,B) and 8(C).

type	thickness (μm)	V_{OC} (mV)	FF (%)	J_{SC} (mA cm^{-2})	PCE (%)	Dye loading (mmol cm^{-3})	L_n/L at 625 mV	η_{COL} (%)
virus-templated TiO_2-only	18.1	801.8	68.6	10.97	6.03	70.9	8.4	99.6
virus-templated Au@TiO_2	15.1	832.7	74.0	13.72	8.46	68.2	7.1	99.4
nanoparticle	17.7	781.1	68.8	12.31	6.63	96.9	1.8	92.0

The effects of AuNPs on the optical absorption of dye-molecules in solution and in the virus-templated thin films are investigated using a UV−vis spectrophotometer. As shown in Figure 6(A−C), the light absorption of dye-molecules in an aqueous solution increases with the presence of AuNPs in the wavelength range 450−530 nm, producing a peak absorption value that is 45% higher than the same dye-solution without AuNPs. The observation that the absorbance of the dye−AuNP mixture is also higher than a pure AuNP solution of the same concentration is attributed to the ability of the AuNPs to concentrate photons in a near-field, which are then converted into charges by neighboring dye-molecules. Similarly, the light absorption of dye-molecules in the virus-templated thin TiO_2 films is increased to a maximum 21% at 540 nm (Figure 6(D−F)), which is also attributed to LSPR. The shifting of the absorption peak from the AuNP solution to a longer wavelength results from the high dielectric constant of the thin TiO_2 layer surrounding the AuNPs and the surrounding porous TiO_2 matrix, which has also been observed in previous reports.[19,20]

To investigate the effect of LSPs on the spectral response of the solar cells, the incident photon-to-current conversion efficiencies (IPCEs) of virus-templated TiO_2-only and Au@TiO_2 photoanodes are compared (Figure 7(A−C)). The IPCE of the plasmon-enhanced DSSC is increased over the entire wavelength range compared to the TiO_2-only DSSC (Figure 7(A)),

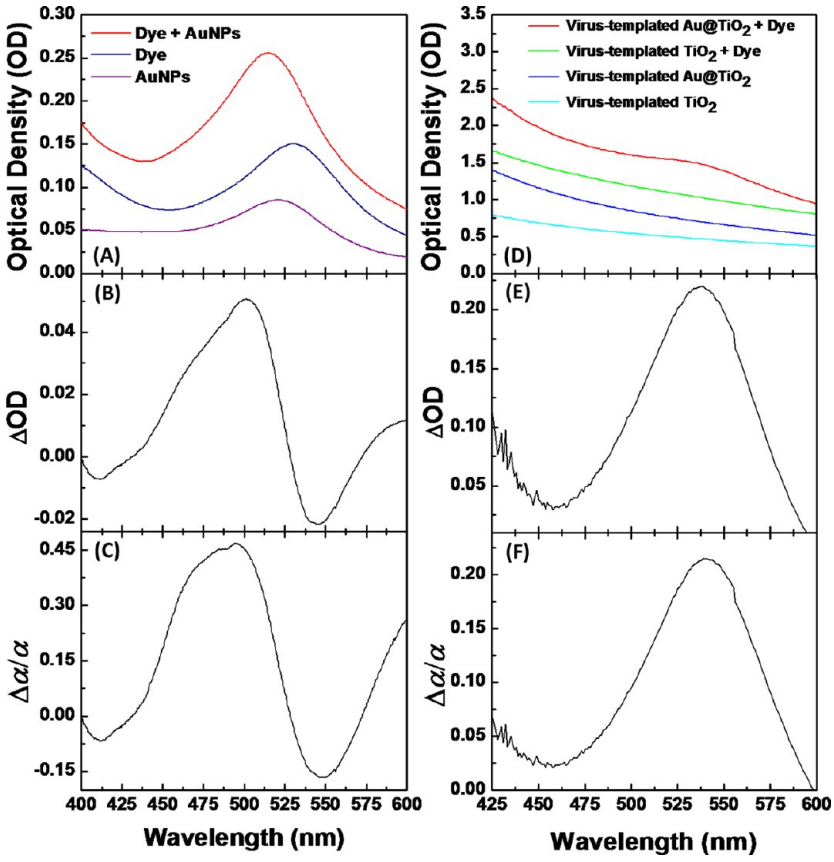

Figure 6. Plasmonic enhancement of optical absorption of dye-molecules in solution and in the virus-templated thin TiO_2 film. (A) Optical absorption spectra of AuNPs, dye-molecules, and their mixture in solution and the concentration of the components (AuNPs and dye-molecules) in all of the solutions are consistent. (B) Net changes of dye absorption (ΔOD) due to the presence of AuNPs in solution. (C) Relative changes of effective extinction coefficient of dye ($\Delta\alpha/\alpha$) due to the presence of AuNPs in solution. (D) Optical absorption spectra of the virus-templated TiO_2 and Au@TiO_2 films and their dye-adsorbed thin films (~0.6 μm). (E) ΔOD of dye due to the presence of AuNPs in thin film. (F) Relative changes of $\Delta\alpha/\alpha$ of dye due to the presence of AuNPs in thin film. For the calculation of ΔOD and $\Delta\alpha/\alpha$: $\Delta\alpha/\alpha = \Delta OD(\lambda)/OD_{dye}(\lambda) = (OD_{dye,Au}(\lambda) - OD_{dye}(\lambda) - OD_{Au}(\lambda))/OD_{dye}(\lambda)$, where $OD_{dye}(\lambda)$, $OD_{Au}(\lambda)$, and $OD_{dye,Au}(\lambda)$ are the optical densities at wavelength λ of pure dye solution, AuNP solution, and their mixture solution with the same concentrations of dye and AuNPs, respectively. For the solid-state thin films, the net absorption of dye-molecule is $OD_{dye}(\lambda) = OD_{dye,TiO2}(\lambda) - OD_{TiO2}(\lambda)$.

indicating that the Au@TiO_2 structures improve light harvesting of the dye-molecules and thus the solar cell. Moreover, the most significant enhancement is in the range 500−600 nm with a peak around 530 nm (from 50.5% to 71.3%, Figure 7(B,C)), in agreement with the absorption enhancement of the thin films.

Device Performance of the Virus-Templated Au@TiO_2 DSSC. The device performance of the virus-templated Au@TiO_2 photoanodes is optimized by varying the concentration of the plasmonic AuNPs and the thickness of the photoanodes (Figure 8(A,B)). The weight fraction (wt %) of AuNPs in the TiO_2 film is examined by X-ray photoelectron spectroscopy (XPS) in Figure S7. In general, thicker photoanodes tend to absorb more light and have higher PCEs and J_{SC}. The virus-templated Au@TiO_2 DSSCs (concentrations of AuNPs, ~0.34 wt % and ~1.03 wt %) always show higher PCE and J_{SC} than the virus-templated TiO_2-only DSSCs with similar photoanode thicknesses. In other words, to achieve the same PCE (*e.g.*, ~6%), the photoanode of the plasmon-enhanced DSSC (6.6 μm) is significantly thinner than that of the TiO_2-only DSSC (18.1 μm), eliminating the need for 63.5% of the photoactive materials used. In addition, both PCE and J_{SC} increase monotonically with the concentration of AuNPs from 0 to 1.03 wt %. However, PCE and J_{SC} decrease when the concentration of AuNPs is increased to 3.09 wt %.

Figure 8(C) and Table 1 show the *J*−*V* characteristics of the most efficient virus-templated plasmon-enhanced DSSC (1.03 wt % AuNP loading) and virus-templated TiO_2-only DSSC. The plasmon-enhanced DSSC achieves a J_{SC} of 13.72 mA cm^{-2}, a 25.1% increase compared to that of the TiO_2-only DSSC, 10.97 mA cm^{-2}. Also, the plasmon-enhanced DSSC shows higher V_{OC} than the TiO_2-only DSSC, which probably results from (1) the reduced charge recombination resulting from thinner photoanodes and (2) a lifted quasi-Fermi level resulting from the equilibrium between the quasi-Fermi level of TiO_2 and the LSP energy level of AuNPs.[18] As expected, the optimized thickness for the LSP-enhanced photoanode (15.1 μm) is thinner than that for the TiO_2-only photoanode (18.1 μm). As a result,

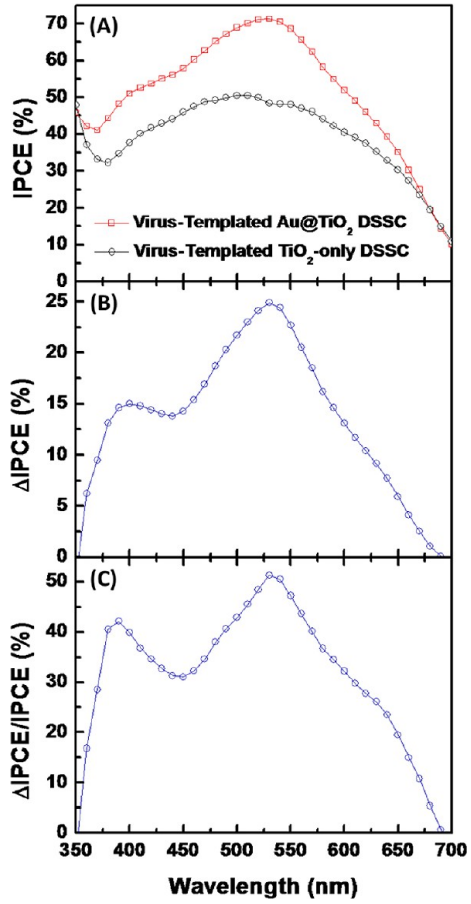

Figure 7. Spectral responses of the virus-templated TiO_2-only and Au@TiO_2 DSSCs. (A) IPCE spectra of the DSSCs with and without the presence of AuNPs. (B) Net change of IPCE (ΔIPCE) and (C) relative changes (ΔIPCE/IPCE) due to the presence of AuNPs. $\Delta IPCE(\lambda)/IPCE = IPCE_{Au@TiO2}(\lambda) - IPCE_{TiO2\text{-}only}(\lambda)/IPCE_{TiO2\text{-}only}(\lambda)$. $IPCE_{Au@TiO2}(\lambda)$ and $IPCE_{TiO2\text{-}only}(\lambda)$ are the IPCE at wavelength λ for the virus-templated Au@TiO_2 and TiO_2-only DSSCs, respectively.

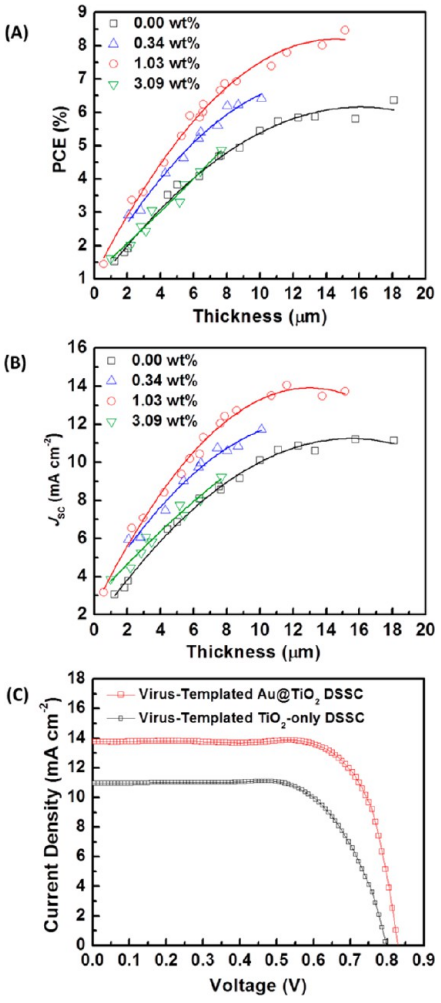

Figure 8. Effect of LSPs on the performance of DSSCs. Dependence of (A) PCE and (B) J_{SC} on the concentration of AuNPs in photoanodes with the different film thickness. (C) $J-V$ curves of the most efficient virus-templated Au@TiO_2 DSSC (AuNP concentration = 1.03 wt %, PCE = 8.46%, FF = 74%, ~15.1 μm) and TiO_2-only DSSC in this work.

the virus-templated plasmon-enhanced DSSC achieves the highest PCE of 8.46%, a 40.3% increase compared to that of the virus-templated TiO_2-only DSSC, 6.03%, while the photoanode thickness is decreased by 19.9%. Moreover, the AuNPs in NW-based photoanodes provide an ability to increase the light harvesting without affecting the high L_n (~7.2 times the film thickness) achieved by the virus-templated NW-based network and, thus, maintain efficient η_{COL} at 99.4% (Figure 4(A) and Table 1).

Computational Model of the Optimal Loading of AuNPs. The experimental data in Figure 8(A,B) demonstrate that (1) there is an optimum AuNP wt % that maximizes PCE and J_{SC} and (2) the shape of the curves for PCE and J_{SC} follow the same trend; therefore, it is reasonable to explain how AuNPs influence PCE by focusing on how they would affect J_{SC}. At the microscopic level, the current produced in the DSSC is generated by the dye-molecules absorbing photons and converting them into electron−hole pairs. Analytically, the flux of photons striking a point in space is proportional to the electric field intensity present there. Therefore, it is expected that the short-circuit current should ultimately be proportional to the electric field intensity integrated over the volume of the device. In the absence of AuNPs, the sunlight incident on the device can be modeled as a simple plane-wave that uniformly illuminates the entire device area. However, when AuNPs are added, each particle acts as an antenna, which concentrates the sunlight within a volume several nanometers from the particle surface. Any dye-molecules that are adsorbed onto a TiO_2 surface and located within the near-field of a NP will experience an enhanced electric field, which is equivalent to being bombarded by a higher photon flux. By numerically evaluating the electromagnetic field produced by metal NPs with finite-difference time-domain (FDTD) simulations, an analytical model has been developed that quantifies the electric field enhancement due to LSPR in a DSSC, which is expected to be proportional to the short-circuit current and overall device efficiency. By modeling the virus-templated

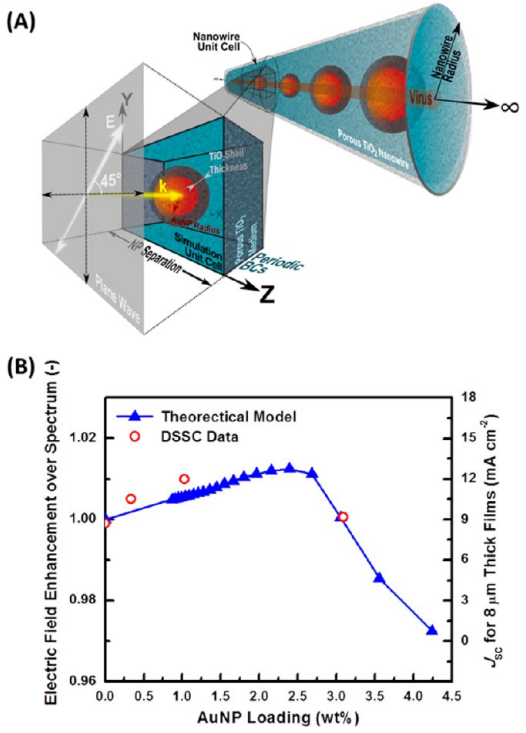

Figure 9. (A) Schematic of the model geometry. The theoretical model idealizes the plasmon-enhanced TiO_2 NWs as an infinite 1D chain of regularly spaced Au@TiO_2 CS NPs that has been encapsulated in a nanoporous TiO_2 cylinder. By using periodic boundary conditions in the *z*-direction, the optical response of the NW can be determined through evaluating only a unit cell containing a single CS with the FDTD method. (B) Dependence of the theoretically predicted optical enhancement of the DSSC devices (left axis) and experimentally measured device J_{SC} (right axis) on AuNP concentration. The device data plotted are for films with 8 μm film thicknesses. The modeling results are specific for a porous NW radius of 90 nm with a TiO_2 volume fraction of 85%, AuNP radius of 10 nm with a 5-nm-thick solid TiO_2 shell, and a plane-wave injected along the *x*-axis with a 45° polarization as shown in part (A).

NWs as infinitely long NWs with Au@TiO_2 core−shells (CSs) embedded in a porous TiO_2-electrolyte matrix (Figure 9(A)), the predicted electric field enhancement *versus* AuNP loading curves follow the same trend as that empirically witnessed for J_{SC} (Figure 9(B)). Therefore, a purely physical explanation is proposed for why an optimal AuNP loading ratio exists for maximizing PCE, which relies solely on Maxwell's equations and reasonable modeling assumptions. Furthermore, the model predicts that light enhancement is maximized for a AuNP loading of 2.4 wt %, which is in good agreement with the experimental data. It is worth noting that the optical response of the linear AuNP chain is dependent upon the polarization of the incident light. However, a polarization of 45° with respect to the NW axis produces the most realistic results because (1) the NWs within the device will be randomly oriented and (2) the spatial incoherence of sunlight will cause the wavetrains to arrive at the solar cell with random polarizations.

The conceptual explanation for the trend shown in Figure 9(B) is as follows: if the particles are spaced at regular intervals far enough apart from one another (*i.e.*, loading fraction is ∼0), the electric near-field surrounding each particle does not interact with that of its neighbor. If the AuNPs are slowly brought closer to one another (*i.e.*, the loading fraction increases), the local electric field profile around each particle remains the same; however more AuNPs are present in the system; thus, the electric field enhancement in the device improves with increasing loading fraction because more dye-molecules are experiencing a higher photon flux. However, if the NPs are brought close enough together that the electric fields surrounding the individual particles interact with one another, the fields become more concentrated in the space between them. Since the NPs are modeled as having a solid TiO_2 shell surrounding them (this empirically must be true, otherwise the gold surface will contact the electrolyte directly and trap charges, thereby promoting recombination), the proximity will cause the near-field to become more concentrated inside the shell itself, which is inaccessible to the dye and the electrolyte. Therefore, the photons that reside there will not contribute to current generation and higher AuNP loadings will result in a subsequent decrease in light absorption by the dye. The analysis presented here is only modeling how the AuNPs enhance the electric field intensity (or equivalently, the photon flux) experienced by the dye-molecules, and no effort has been made to explain how photocharges are generated, transported, or collected by the device. Therefore, only conclusions about the trends can be drawn when comparing the optical enhancement predictions and the J_{SC} data shown in Figure 9(B).

CONCLUSION

In summary, the M13 bacteriophage has been successfully demonstrated as a biotemplate to create a dual-functional 3D NW-based porous DSSC photoanode with efficient electron collection and improved light harvesting. The synthesized virus-templated photoanode is composed of photoactive TiO_2 NWs, which provided a direct pathway for electron collection and achieved a longer L_n than the traditional NP-based morphology. The affinity of the viral surface proteins for AuNPs enables the formation of plasmonic AuNP−virus complexes capable of improving light harvesting. We have both theoretically predicted and experimentally verified how the phenomenon of LSPR enhances the optical absorption of dye-molecules in the devices. The theoretically predicted trend of how light enhancement should vary with AuNP loading is in excellent agreement with the observed trends of PCE and J_{SC} in the tested devices. Of the devices tested, a maximum PCE of 8.46% is observed for a AuNP loading of 1.03 wt %. In addition to being a relatively low-cost,

aqueous-based synthetic process, it is expected to be scalable to large-scale production, and the device morphology is expected to be useful in other energy-related applications, such as supercapacitors, lithium ion batteries, and water splitting, owing to its ability to rapidly transport electrons and its potential to incorporate different functional materials into the virus-templated NW-based network *via* protein recognition.

MATERIALS AND METHODS

Materials. A 50 wt % glutaraldehyde solution, titanium(IV) chloride ($TiCl_4$), hydrogen tetrachloroaurate ($HAuCl_4$), sodium citrate, acetonitrile, *tert*-butanol, and a phosphate-buffered saline (PBS) solution were purchased from Sigma Aldrich. Ammonium hexafluorotitanate ($(NH_4)_2TiF_6$) and boric acid (H_3BO_3) were purchased from Alfa Aesar. *cis*-(Diisothiocyanato)bis(2,2′-bipyridyl-4,4′-dicarboxylato)ruthenium(II) bis(tetrabutylammonium) (also named N719) and TiO_2 NP paste (13/400 nm, Ti-Nanoxide D/SP) were purchased from Solaronix. N719 dye solution was prepared in an acetonitrile and *tert*-butanol (volume ratio 1:1) mixture at 0.5 mM. All reagents were used as received and without further purification. All water was deionized (18.2 MΩ, Mill-Q pore). The virus solution consisting of the E3M13 bacteriophage (AEEE peptide expressed on the pVIII major coat protein) was diluted to 5×10^{13} phage mL^{-1} with PBS buffer.

Synthesis of AuNPs. The AuNP solution was prepared by the following procedure: 10 mg of $HAuCl_4$ was initially dissolved in 100 mL of water, and the solution was heated to boiling. Then 50 mg of sodium citrate was dissolved in 5 mL of water, and the solution was added into the boiling $HAuCl_4$ solution under vigorous stirring. The mixed solution was reacted at boiling for 30 min. The synthesized AuNP solution was stored at 4 °C.

Binding AuNPs on M13 Virus. The different amounts of phage solution were mixed with AuNP solution and then incubated in dark conditions at 4 °C for 12 h. Then, Au−virus was precipitated through the standard polyethylene glycol and sodium chloride solution to minimize the impurities. The final pellet was redissolved and diluted to 5×10^{13} phage mL^{-1} with PBS buffer. The synthesized AuNP−virus solution was stored at 4 °C.

M13 Virus Hydrogel. On an FTO glass substrate, an area of 1 cm × 1 cm was defined using a 25-μm-thick Surlyn film (Solaronix Meltonix 1170-25), which was attached onto the FTO substrate by melting at 120 °C for 15 min. A 10 μL sample of virus solution or Au−virus solution was then dropped on the FTO. The FTO with the virus solution was inverted and put on top of a solution of 50% glutaraldehyde, which served as a cross-linking agent. The cross-linking reaction was allowed to proceed for 2 h. Afterward, the resulting virus hydrogels (along with the FTO substrate) were removed from the cross-linking solution and transferred to a PBS buffer to remove excess glutaraldehyde in the hydrogel overnight.

TiO_2 Photoanode Generation. The cross-linked phage hydrogels were immersed in a 0.2 M $TiCl_4$ solution for ∼6 h and in a mixture of 30 mM $(NH_4)_2TiF_6$ and H_3BO_3 for 4 h at 50 °C subsequently for TiO_2 nucleation. After nucleation, the films were rinsed with water and then annealed at 500 °C for 30 min. Thicker films were achieved by repeating the fabrication process (cross-linking, nucleation, and calcination). For the NP-based photoanodes, layers of commercial TiO_2 NP paste were doctor-bladed on the substrates and then annealed at 500 °C for 15 min. Film thickness was monitored using a surface profilometer (Veeco Dektak). SEM images of the film morphology were obtained using a Helios Nanolab 600 dual-beam focused ion beam system. TEM observations of synthesized nanostructures were performed using a JEOL 200CX TEM with an accelerating voltage of 120 kV and a JEOL 2010 TEM with an accelerating voltage of 200 kV. The optical absorption spectroscopy measurements were performed using a Beckman Coulter DU800 UV−vis spectrophotometer. XPS measurement with a scanning monochromated Al source (spot size 200 μm) determined the composition of the film. A depth profiling analysis was performed, sputtering with an argon source for 740 min, or approximately 1.5 μm in depth.

Fabrication of DSSCs. After calcination, the photoanodes were cooled to 80 °C, immersed in the N719 solution, and kept at room temperature over 24 h. The counter-electrode was a 100-nm-thick platinum film sputtered on an FTO substrate. The electrolyte employed was a solution of 0.6 M 1-butyl-3-methylimidazolium iodide (Sigma Aldrich), 0.03 M I_2 (Sigma Aldrich), 0.10 M guanidinium thiocyanate (Sigma Aldrich), and 0.5 M 4-*tert*-butylpyridine (Sigma Aldrich) in a mixture of acetonitrile and valeronitrile (volume ratio 85:15).[28] The dyed TiO_2 photoanodes and platinum counter-electrodes were assembled into a sandwich-type cell and sealed with a hot-melt 25 μm Surlyn. The final photoanode had dimensions of ∼0.16 cm^2 (4 mm × 4 mm), further determined from a calibrated digital camera image.

Characterization of DSSCs. Photovoltaic measurements were performed using an AM 1.5 solar simulator (Photo Emission Tech.). The power of the simulated light was calibrated to 100 mW cm^{-2} by using a reference silicon photodiode with a power meter (1835-C, Newport) and a reference silicon solar cell to reduce the mismatch between the simulated light and AM 1.5. *J*−*V* curves were obtained by applying an external bias to the cell and measuring the generated photocurrent with a Keithley model 2400 digital source meter. The voltage step and delay time of the photocurrent were 10 mV and 40 ms, respectively. The dye loading of the photoanode was determined by eluting the N719 dye from the TiO_2 electrode into a known amount of 0.1 M NaOH and using a UV−vis calibration curve to determine the concentration of dye in solution to total amount of dye per film volume. IPCE spectra were obtained with a computer-controlled system (model QEX7, PV Measurements, Inc.) consisting of a 150 W xenon lamp light source and a monochromator with two 1200 g/mm diffraction gratings. The monochromator was incremented through the wavelength range from 350 to 900 nm to generate the spectral response of IPCE with a spectral resolution of 10 nm. The incident photon flux was determined using a calibrated silicon photodiode (calibrated by PV Measurements, Inc.). Measurements were performed in a short-circuit condition, while the cell was under background illumination from a bias light of 50 mW cm^{-2}. Bias illumination was from the same direction as the monochromatic light, which was from the FTO side. The monochromatic beam was chopped using a computer-controlled shutter at a frequency of 4 Hz, and averaging of up to 40 shutter cycles was employed. EIS of DSSCs were measured using a Solartron 1260 frequency response analyzer. The obtained impedance spectra were fit to the transmission line model with Z-view software (v3.2b, Scribner Associates).[29] The spectra were measured at various forward bias voltages (from 0.85 to 0.45 V) in the frequency range ∼0.1 Hz to ∼1 MHz with oscillation potential amplitudes of 10 mV at room temperature. The photoanode was connected to the working electrode. The platinum electrode was connected to the auxiliary electrode and reference electrodes. The impedance measurements were carried out at forward bias in dark conditions.

Theoretical Modeling. The optical properties of the DSSC system were theoretically investigated using the FDTD method with the software Lumerical FDTD Solutions version 8.0.0. The plasmon-enhanced TiO_2 NW morphology of the DSSC was modeled as an infinitely long nanoporous TiO_2 NW with a radius of 90 nm, which encapsulated a periodic 1D chain of AuNP-TiO_2 CSs, as shown in Figure 9(A). Placing periodic boundary conditions along the *z*-direction allowed the simulation volume to be dramatically reduced to a unit cell containing a single 20-nm-diameter AuNP with a 5-nm-thick, solid TiO_2 shell. The medium surrounding the CS NP was modeled as a nanoporous TiO_2/water matrix with an effective index of 2.148, which was calculated for a TiO_2 volumetric fill fraction of 85% (based on TEM

images) using effective medium theory.[30] It was inherently assumed here that the dye-molecules would be able to infiltrate into all the pores of the TiO_2 NW and thus be uniformly distributed across the volume. Multiple simulations were performed with center-to-center NP separation periods ranging from 20 to 100 nm. Each unit-cell simulation domain was illuminated by a plane-wave with a polarization oriented 45° to the NW axis at 400 different wavelengths between 350 and 900 nm. A fourth-order polynomial was fitted over this wavelength range to the measured dielectric data of gold as reported by Palik.[31] The refractive index of solid TiO_2 was approximated as 2.34 and taken to be constant over the wavelengths of interest. This value was found by averaging the dispersion relation reported by Kim[32] between the wavelengths of 350 and 950 nm.

For each simulation geometry, an enhancement factor was calculated that compares the amount of light intensity available for absorption by the dye-molecules distributed throughout the TiO_2 NW matrix with and without the AuNP-TiO_2 CS NPs:

$$\text{Enhancement Factor} = \frac{\text{Total Electric Field Intensity in Plasmonic NW Unit Cell}}{\text{Total Electric Field Intensity in NW Unit Cell without AuNPs}} = \frac{\int_{\lambda_{min}}^{\lambda_{max}} \left(\iiint_{\substack{Volume\ of\ NW \\ Unit\ Cell\ Outside \\ CS\ Surface}} |E(x,y,z,\lambda)|^2\, dV \right) d\lambda}{\int_{\lambda_{min}}^{\lambda_{max}} \left(\iiint_{Volume\ of\ NW\ Unit\ Cell} |E_0(x,y,z,\lambda)|^2\, dV \right) d\lambda}$$

where E is the electric field for the model with the AuNP-TiO_2 CSs, E_0 is the electric field of the incident plane wave, and the "Volume of NW Unit Cell" refers to a cylindrical slice through the porous TiO_2 NW that is centered about a single AuNP-TiO_2 CS with a width equal to the NP separation distance (Figure 9(A)). It is worth emphasizing that the enhancement factor is defined to calculate the overall light enhancement that the dye-molecules loaded into the porous TiO_2 NW experience because the dye is what ultimately generates charges in the system. Therefore, the electric field located within the solid TiO_2 shell and the inside the AuNP core do not contribute to the above volume integral because that space is inaccessible to the dye.

The weight fraction of AuNPs in the DSSC system is defined as

$$\text{AuNP wt } \% = \frac{M_{AuNPs}}{M_{AuNPs} + M_{TiO_2}} \times 100$$

where M_{AuNPs} is the mass of the AuNPs in the system and M_{TiO_2} is the total mass of the TiO_2 in the system, which includes the material in the thin solid shell surrounding the AuNP as well as the material in the porous TiO_2/water matrix that makes up the NW volume.

Conflict of Interest: The authors declare no competing financial interest.

Acknowledgment. This work was supported by Eni, S.p.A (Italy) through the MIT Energy Initiative Program. N.F. acknowledges support by NSF (ECCS Award No. 1028568) and by the Air Force Office of Scientific Research (AFOSR MURI Award No. FA9550-12-1-0488). M.T.K. acknowledges support from the MIT Energy Initiative Eni-MIT Energy Fellowship. This work made use of the MIT MRSEC Shared Experimental Facilities supported by the National Science Foundation under award number DMR-0819762. P.-Y.C., X.D., F.J.B., P.T.H., and A.M.B. conceived the idea and designed the experiments. P.-Y.C. performed the synthesis and SEM imaging. P.-Y.C. and J.Q. performed the TEM imaging. P.-Y.C., X.D., and J.Q. performed the fabrication and characterization of the solar cells. M.T.K. and N.F. performed the numerical modeling study. N.-M.D.C. performed the XPS measurement. P.-Y.C., X.D., M.T.K., P.T.H., and A.M.B. co-wrote the paper, and all authors discussed the results and commented on the manuscript. The authors wish to dedicate this paper to the memory of Officer Sean Collier, for his caring service to the MIT community and for his sacrifice.

Supporting Information Available: SEM images of the virus-templated photoanodes with/without TiO_2 nucleation by $(NH_4)_2TiF_6/H_3BO_3$ solution, SEM images of the virus-templated photoanodes nucleated in different concentrations of $TiCl_4$ solution, XRD analysis of TiO_2 nanocrystallites after the hydrolysis of $TiCl_4$, calculation of electron diffusion length and electron collection efficiency, SEM image of the Au@TiO_2 virus-templated film, XPS measurement of the Au@TiO_2 virus-templated film, and details about the theoretical modeling study are provided. This material is available free of charge *via* the Internet at http://pubs.acs.org.

REFERENCES AND NOTES

1. Huang, Y.; Chiang, C.-Y.; Lee, S. K.; Gao, Y.; Hu, E. L.; Yoreo, J. D.; Belcher, A. M. Programmable Assembly of Nanoarchitectures Using Genetically Engineered Viruses. *Nano Lett.* **2005**, *5*, 1429–1434.
2. Whaley, S. R.; English, D. S.; Hu, E. L.; Barbara, P. F.; Belcher, A. M. Selection of Peptides with Semiconductor Binding Specificity for Directed Nanocrystal Assembly. *Nature* **2000**, *405*, 665–668.
3. Arter, J. A.; Taggart, D. K.; McIntire, T. M.; Penner, R. M.; Weiss, G. A. Virus-PEDOT Nanowires for Biosensing. *Nano Lett.* **2010**, *10*, 4858–4862.
4. Dang, X.; Yi, H.; Ham, M.-H.; Qi, J.; Yun, D. S.; Ladewski, R.; Strano, M. S.; Hammond, P. T.; Belcher, A. M. Virus-Templated Self-Assembled Single-Walled Carbon Nanotubes for Highly Efficient Electron Collection in Photovoltaic Devices. *Nat. Nanotechnol.* **2011**, *6*, 377–384.
5. Chung, W.-J.; Oh, J.-W.; Kwak, K.; Lee, B. Y.; Meyer, J.; Wang, E.; Hexemer, A.; Lee, S.-W. Biomimetic Self-Templating Supramolecular Structures. *Nature* **2011**, *478*, 364–368.
6. Neltner, B.; Peddie, B.; Xu, A.; Doenlen, W.; Durand, K.; Yun, D. S.; Speakman, S.; Peterson, A.; Belcher, A. Production of Hydrogen Using Nanocrystalline Protein-Templated Catalysts on M13 Phage. *ACS Nano* **2010**, *4*, 3227–3235.
7. Liu, Y.; Zhang, W.; Zhu, Y.; Luo, Y.; Xu, Y.; Brown, A.; Culver, J. N.; Lundgren, C. A.; Xu, K.; Wang, Y.; Wang, C. Architecturing Hierarchical Function Layers on Self-Assembled Viral Templates as 3D Nano-Array Electrodes for Integrated Li-Ion Microbatteries. *Nano Lett.* **2012**, *13*, 293–300.
8. Lee, Y. J.; Yi, H.; Kim, W.-J.; Kang, K.; Yun, D. S.; Strano, M. S.; Ceder, G.; Belcher, A. M. Fabricating Genetically Engineered High-Power Lithium-Ion Batteries Using Multiple Virus Genes. *Science* **2009**, *324*, 1051–1055.
9. Nuraje, N.; Dang, X.; Qi, J.; Allen, M. A.; Lei, Y.; Belcher, A. M. Biotemplated Synthesis of Perovskite Nanomaterials for Solar Energy Conversion. *Adv. Mater.* **2012**, *24*, 2885–2889.
10. Chen, P.-Y.; Ladewski, R.; Miller, R.; Dang, X.; Qi, J.; Liau, F.; Belcher, A. M.; Hammond, P. T. Layer-by-Layer Assembled Porous Photoanodes for Efficient Electron Collection in Dye-Sensitized Solar Cells. *J. Mater. Chem. A* **2013**, *1*, 2217–2224.
11. Lee, Y. M.; Kim, Y. H.; Lee, J. H.; Park, J. H.; Park, N.-G.; Choe, W.-S.; Ko, M. J.; Yoo, P. J. Highly Interconnected Porous Electrodes for Dye-Sensitized Solar Cells Using Viruses as a Sacrificial Template. *Adv. Funct. Mater.* **2011**, *21*, 1160–1167.
12. Yella, A.; Lee, H.-W.; Tsao, H. N.; Yi, C.; Chandiran, A. K.; Nazeeruddin, M. K.; Diau, E. W.-G.; Yeh, C.-Y.; Zakeeruddin, S. M.; Grätzel, M. Porphyrin-Sensitized Solar Cells with Cobalt (II/III)-Based Redox Electrolyte Exceed 12% Efficiency. *Science* **2012**, *334*, 629–634.
13. Hagfeldt, A.; Boschloo, G.; Sun, L.; Kloo, L.; Pettersson, H. Dye-Sensitized Solar Cells. *Chem. Rev.* **2010**, *110*, 6595–6663.
14. Kang, S. H.; Choi, S. H.; Kang, M. S.; Kim, J. Y.; Kim, H. S.; Hyeon, T.; Sung, Y. E. Nanorod-Based Dye-Sensitized Solar Cells with Improved Charge Collection Efficiency. *Adv. Mater.* **2008**, *20*, 54–58.
15. Zheng, Q.; Kang, H.; Yun, J.; Lee, J.; Park, J. H.; Baik, S. Hierarchical Construction of Self-Standing Anodized Titania Nanotube Arrays and Nanoparticles for Efficient and Cost-Effective Front-Illuminated Dye-Sensitized Solar Cells. *ACS Nano* **2011**, *5*, 5088–5093.

16. Kunal, M.; Tai-Hou, T.; Rajan, J.; Seeram, R. Electron Transport in Electrospun TiO_2 Nanofiber Dye-Sensitized Solar Cells. *Appl. Phys. Lett.* **2009**, *95*, 012101.
17. Brown, M. D.; Suteewong, T.; Kumar, R. S. S.; D' Innocenzo, V.; Petrozza, A.; Lee, M. M.; Wiesner, U.; Snaith, H. J. Plasmonic Dye-Sensitized Solar Cells Using Core-Shell Metal-Insulator Nanoparticles. *Nano Lett.* **2010**, *11*, 438–445.
18. Choi, H.; Chen, W. T.; Kamat, P. V. Know Thy Nano Neighbor. Plasmonic *versus* Electron Charging Effects of Metal Nanoparticles in Dye-Sensitized Solar Cells. *ACS Nano* **2012**, *6*, 4418–4427.
19. Dang, X.; Qi, J.; Klug, M. T.; Chen, P.-Y.; Yun, D. S.; Fang, N. X.; Hammond, P. T.; Belcher, A. M. Tunable Localized Surface Plasmon-Enabled Broadband Light-Harvesting Enhancement for High-Efficiency Panchromatic Dye-Sensitized Solar Cells. *Nano Lett.* **2013**, *13*, 637–642.
20. Qi, J.; Dang, X.; Hammond, P. T.; Belcher, A. M. Highly Efficient Plasmon-Enhanced Dye-Sensitized Solar Cells through Metal@Oxide Core-Shell Nanostructure. *ACS Nano* **2011**, *5*, 7108–7116.
21. Migneault, I.; Dartiguenave, C.; Bertrand, M. J.; Waldron, K. C. Glutaraldehyde: Behavior in Aqueous Solution, Reaction with Proteins, and Application to Enzyme Crosslinking. *BioTechniques* **2004**, *37*, 790–802.
22. Zhang, Q.; Gao, L.; Guo, J. Effects of Calcination on the Photocatalytic Properties of Nanosized TiO_2 Powders Prepared by $TiCl_4$ Hydrolysis. *Appl. Catal., B* **2000**, *26*, 207–215.
23. Ni, M.; Leung, M. K. H.; Leung, D. Y. C.; Sumathy, K. An Analytical Study of the Porosity Effect on Dye-Sensitized Solar Cell Performance. *Sol. Energy Mater. Sol. Cells* **2006**, *90*, 1331–1344.
24. Hutter, E.; Fendler, J. H. Exploitation of Localized Surface Plasmon Resonance. *Adv. Mater.* **2004**, *16*, 1685–1706.
25. Atwater, H. A.; Polman, A. Plasmonics for Improved Photovoltaic Devices. *Nat. Mater.* **2010**, *9*, 205–213.
26. Schuller, J. A.; Barnard, E. S.; Cai, W.; Jun, Y. C.; White, J. S.; Brongersma, M. L. Plasmonics for Extreme Light Concentration and Manipulation. *Nat. Mater.* **2010**, *9*, 193–204.
27. Wu, J.-L.; Chen, F.-C.; Hsiao, Y.-S.; Chien, F.-C.; Chen, P.; Kuo, C.-H.; Huang, M. H.; Hsu, C.-S. Surface Plasmonic Effects of Metallic Nanoparticles on the Performance of Polymer Bulk Heterojunction Solar Cells. *ACS Nano* **2011**, *5*, 959–967.
28. Ito, S.; Murakami, T. N.; Comte, P.; Liska, P.; Grätzel, C.; Nazeeruddin, M. K.; Grätzel, M. Fabrication of Thin Film Dye Sensitized Solar Cells with Solar to Electric Power Conversion Efficiency Over 10%. *Thin Solid Films* **2008**, *516*, 4613–4619.
29. Halme, J.; Vahermaa, P.; Miettunen, K.; Lund, P. Device Physics of Dye Solar Cells. *Adv. Mater.* **2010**, *22*, E210–E234.
30. Bohren, C. F.; Huffman, D. R. *Absorption and Scattering of Light by Small Particles*; Wiley-Interscience: New York, 1998.
31. Palik, E. D. *Handbook of Optical Constants of Solids*; Elsevier, 1998.
32. Kim, S. Y. Simultaneous Determination of Refractive Index, Extinction Coefficient, and Void Distribution of Titanium Dioxide Thin Film by Optical Methods. *Appl. Opt.* **1996**, *35*, 6703–6707.